JCTC Journal of Chemical Theory and Computation

Article

pubs.acs.org/JCTC

Joint Use of Bonding Evolution Theory and QM/MM Hybrid Method for Understanding the Hydrogen Abstraction Mechanism via Cytochrome P450 Aromatase

Ignacio Viciano, Patricio González-Navarrete, Juan Andrés,* and Sergio Martí

Departament de Química Física i Analítica, Universitat Jaume I, 12071, Castellón, Spain

Supporting Information

ABSTRACT: Bonding evolution theory (BET), as a combination of the electron localization function (ELF) and Thom's catastrophe theory (CT), has been coupled with quantum mechanics/molecular mechanics (QM/MM) method in order to study biochemical reaction paths. The evolution of the bond breaking/forming processes and electron pair rearrangements in an inhomogeneous dynamic environment provided by the enzyme has been elucidated. The proposed methodology is applied in an enzymatic system in order to clarify the reaction mechanism for the hydrogen abstraction of the androstenedione (ASD) substrate catalyzed by the cytochrome P450 aromatase enzyme. The use of a QM/MM Hamiltonian allows inclusion of the polarization of the charges derived from the amino acid residues in the wave function, providing a more accurate and realistic description of the chemical process. The hydrogen abstraction step is found to have five different ELF structural stability domains, whereas the C−H breaking and O−H forming bond process rearrangements are taking place in an asynchronous way.

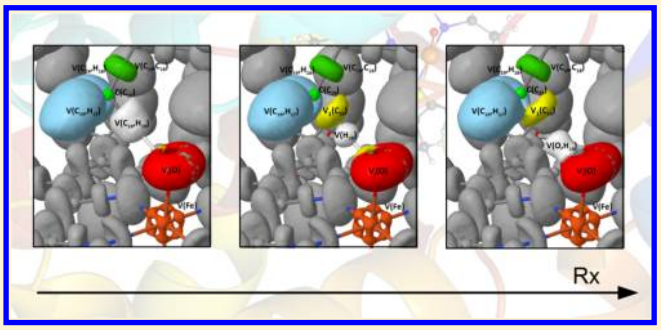

1. INTRODUCTION

In most of the theoretical studies on chemical reactivity, relevant insights into the electronic structure are based on the localization of minimum energy reaction pathways between stable configurations on a high-dimensional potential energy surface (PES). This energy-based representation provides a wealth of information on the chemical reactivity; however, energy as a global quantity misses mechanistic details such as bond breaking/forming processes that are the essence of chemical reactivity.

Since the chemical reaction can be described as a sequence of events of a complex process in space and time, an adequate representation of these chemical events should be given by a physical observable. The electron density, $\rho(r)$, meets these requirements which can be achieved by Bader's quantum theory of atoms in molecules (QTAIM).[1] This analysis affords a rigorous and exact definition of bonding within an atomic ensemble in terms of topological properties of the $\rho(r)$.[1] Likewise, QTAIM provides a partition of the geometrical space occupied by the chemical system into adjacent nonoverlapping volumes called "basins", which can be thought as chemical entities such as atoms in molecules. Thus, determining the electron densities of all atoms can lead to establishing the evolution of the connectivity among them, while an energy-based representation associated with an accurate description of the electronic density along the reaction coordinate can provide a valuable notion about the reaction mechanism. In consequence, the methods which involve the analysis of $\rho(r)$ should have a particular appeal for chemists contributing to understanding the electronic structures of molecular processes and the chemical reactivity.[1]

One of the most popular alternative partitions of the molecular space is provided by the topological analysis of the electron localization function (ELF), originally introduced by Becke and Edgecombe.[2] ELF can be understood as a local measure of the Pauli repulsion between electrons due to the exclusion principle, which allows defining regions of space that are associated with different electron pairs in a molecule.[3] In this sense, the topological analysis of the ELF can also be treated as a continuous and differentiable scalar field in three-dimensional space which provides information on the structure of atomic shells, location, size of bonding, and lone electron pairs.[4] Popelier proposed that these type of studies, based on the topological analysis of $\rho(r)$ and its related scalar field, form a unified theoretical framework, named "quantum chemical topology" (QCT), inspired by the seminal work of Bader.[5] QCT provides a bridge between the traditional scheme of the chemical bond derived from the Lewis theory and first-principles quantum-mechanical methodologies.

Hybrid schemes based on quantum mechanics/molecular mechanics (QM/MM) are well-established computational techniques to describe theoretically the electronic structures in biochemical reactions taking into account the effects of

Received: November 19, 2014
Published: February 20, 2015

DOI: 10.1021/ct501030q
J. Chem. Theory Comput. 2015, 11, 1470−1480

environment.[6] The use of the topological analysis of the ELF has been successfully applied to large biological systems treated at the QM/MM level of theory, demonstrating its applicability in this kind of macromolecular entity.[7] A further step is to take into account René Thom's catastrophe theory (CT)[8] coupled with ELF, i.e., the use of bonding evolution theory (BET).[8a] The mathematical foundations, as well as a number of cases where BET has been successfully applied, have been reviewed comprehensively in recent times.[9] Since the topological behavior of the ELF gradient field can be studied within the framework provided by CT, BET allows finding a direct relationship between the ELF topology and the evolution of the bond breaking/forming processes and electron pair rearrangements as the chemical reaction proceeds.

In the present work, the joint use of the BET methodology with the QM/MM hybrid scheme has been applied in order to study the hydrogen abstraction process catalyzed by the cytochrome P450 aromatase enzyme. This biomolecule is a member of the superfamily of cytochrome P450 metalloenzymes (CYP19A1) and is uniquely known to be able to catalyze the biosynthesis of estrogens from androgens in humans.[10] Since this enzyme is responsible for the final (and rate-limiting) step of estrogen formation, it has aroused considerable interest in the field of endocrinology due to its success as a therapeutic target in the treatment of hormone-dependent breast cancer.[11] The most important reactions catalyzed by aromatase are the conversion of androstenedione (ASD) (Scheme 1) and testosterone to estrone and estradiol[12]

Scheme 1. Structure of the Androstenedione Substrate

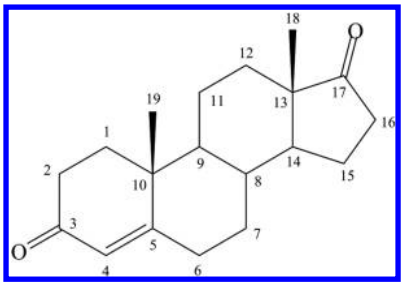

respectively via a three-step oxidative transformation (see Scheme 2). The first and second steps are accepted to be sequential hydroxylation of the C_{19}-methyl via the classical oxygen rebound mechanism that leads to the formation of the C_{19}-aldehyde (or C_{19}-oxo-ASD). The third "lyase" step (which is still controversial) culminates in the cleavage of the $C_{10}-C_{19}$ bond of the C_{19}-oxo-ASD, leading to the aromatization of the steroid A-ring of androgens and expelling the C_{19} as formic acid.[13]

During the first oxidation step of ASD via the enzyme aromatase, the P450-mediated hydrogen atom abstraction–oxygen rebound mechanism originally proposed by Groves and co-workers[14] takes place. Along this step, three substages can be distinguished as can be seen in Scheme 3:

(i) → (ii) An inert C–H bond of the substrate is activated by means of the high valent ferryl–oxo species commonly referred to as Compound I (Cpd I), leading to the formation of the alkyl radical intermediate and the iron–hydroxo complex.

(ii) → (iii) A reorientation (rotation) of the alkyl group and the OH radical takes place in order to prepare the oxygen rebound mechanism.

(iii) → (iv) A recombination of radical intermediate with the iron-bound hydroxyl radical leads to the formation of a new C–O bond (hydroxylated substrate).

Recently, the electronic structure of Cpd I (Fe(IV)–oxo porphyrin π-cation radical) was studied in our research group[15] by means of the analysis of the ELF and the electron density. Cpd I has a radical nature due to three single occupied orbitals (two orbitals forming a local triplet focused on the Fe–O moiety, and one delocalized between the A_{2u} orbital of the porphyrin and the π_s of the sulfur atom). Depending on the coupling of these three electrons, Cpd I can adopt two different close-lying spin configurations: doublet (low spin) or quartet (high spin). For this reason, Shaik and co-workers[16] have proposed a two-state reactivity mechanism (TSR)[17] for the oxidation reactions carried out by cytochrome P450 enzymes. In our previous work, the interaction of the central iron atom with its coordinated ligands, as well as the structure of the carbon–carbon bonds in porphyrin moiety, was studied, providing deeper insights into the nature of the bonds and the electronic distribution of Cpd I.

Herein, we present an alternative representation of the electron density redistribution for the hydrogen abstraction process of the ASD substrate via the enzyme aromatase, at two competing doublet and quartet spin state surfaces. We provide the first study where the BET[8a] has been used in a large biological system, employing electronic wave functions obtained from QM/MM calculations, thus incorporating the polarization effect of the charges derived from the enzymatic environment. The strategy adopted in this research provides a new insight into the electronic structure and related properties of the stationary points along the PES, enabling a nice guide to elucidate the mechanism of this biochemical process. Using this procedure, we are able to answer the following questions: (i) How could the electronic reorganization proceed along the reaction path? (ii) Is the electron density flowing synchronously, and in which direction? (iii) When and how do the bond formation/breaking processes along the reaction path take place? (iv) Does the formation/rupture of bonds take place before or after the transition structure (TS) is reached?

2. COMPUTATIONAL DETAILS

2.1. Obtaining QM/MM Potential Energy Surfaces. The initial geometry of the human placental aromatase (CYP19A1) in complex with its natural substrate androstenedione was obtained from the X-ray crystal structure (PDB code 3EQM).[18] The iron pentacoordinated heme species was manually modeled into a hexacoordinated iron–oxo porphyrin, Cpd I. The protonation states of the residues were carefully defined according to the pK_a values obtained with the PROPKA web interface.[19] All the hydrogen atoms were added using the fDYNAMO[20] library, and a total of four counterions (Cl^-) were placed into electrostatically favorable positions around the enzyme in order to electroneutralize the excess of positive charge. Subsequently, the system was placed in a prerelaxed orthorhombic box of water molecules with dimensions of 90 Å × 80 Å × 80 Å. The resulting model consisted of 452 residues of amino acids, the modeled Cpd I, the substrate ASD, 4 counterions, 35 crystallographic water molecules, and 16 542 water molecules of the solvation box.

A semiempirical QM/MM relaxation of this model was carried out using the AM1[21] Hamiltonian for the ASD substrate, and the OPLS-AA[22]/TIP3P[23] force field. Then, the resulting structure was equilibrated by means of hybrid

DOI: 10.1021/ct501030q
J. Chem. Theory Comput. 2015, 11, 1470–1480

Scheme 2. Catalytic Process of Conversion of Androgens into Aromatic Estrogens Catalyzed by Aromatase

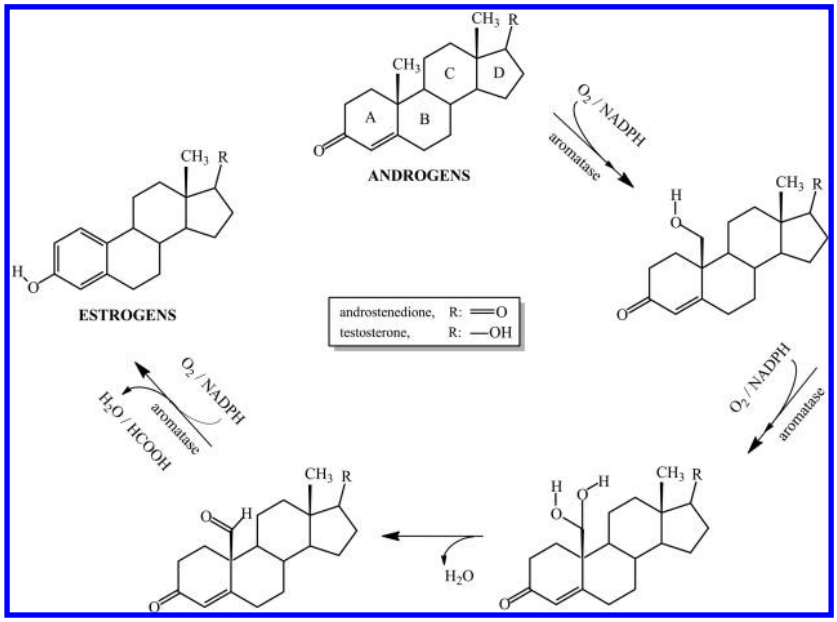

Scheme 3. Hydroxylation of Substrates via Cytochrome P450

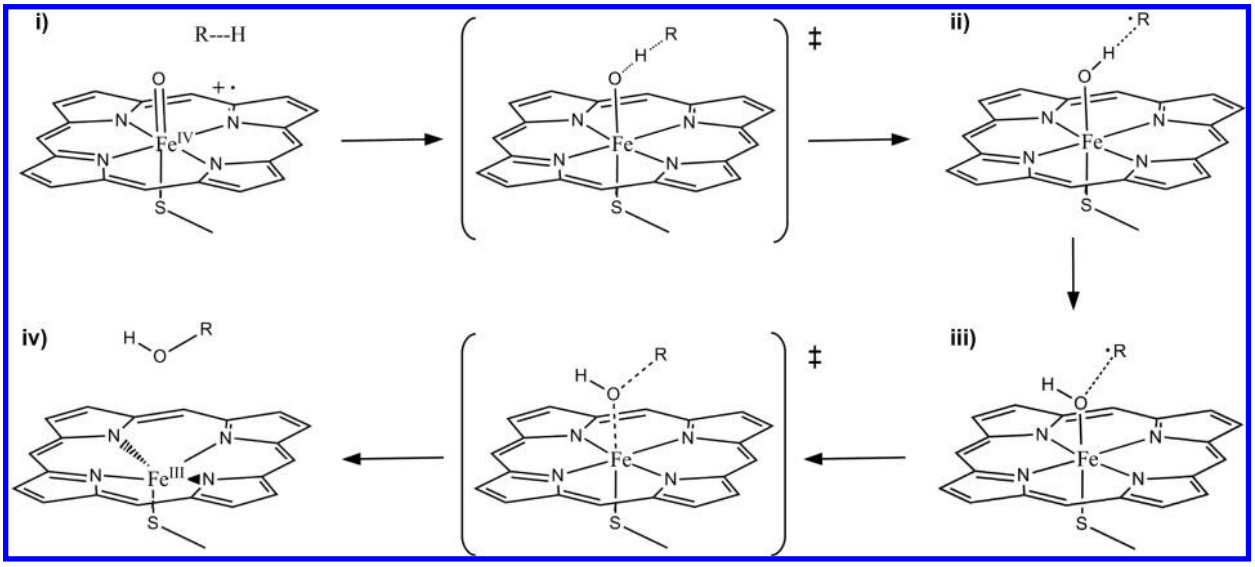

molecular dynamics (MD) at 300 K, using the NVT ensemble and the Langevin−Verlet integrator. The MD was run for 200 ps with a step size of 1 fs, keeping frozen any atom 20 Å apart from the Cpd I or the substrate during all the simulations.

Once the system was equilibrated, the PES was explored for the hydrogen abstraction reaction in both doublet and quartet spin states. The QM region of the model consisted of the substrate androstenedione, Cpd I, and the axial Cys-437 ligand (comprising the S_γ, the C_β, and two H_β atoms), yielding a total amount of 124 atoms, as shown in Figure 1. The link atom[6b] procedure was applied to satisfy the valence of the QM region, due to the presence of the classical bond partitioning in the Cys-437 amino acid (C_α−C_β bond).

The transition structures corresponding to doublet and quartet spin states were localized and characterized as saddle points of order 1 by means of a micro−macro iteration optimization scheme.[24] In this method, the system is divided into two parts: the core or control space, and the environment or complementary space. The Hessian matrix is calculated explicitly only for those atoms belonging to the core. Thus, before each step of the control space Hessian guided optimization (based on the Baker algorithm[25a,b]), the degrees of freedom of the environment are optimized in order to maintain an approximately zero gradient and to minimize the potential energy (using the L-BFGS procedure[25c]). In our case, the core region matches up with the QM region described above. Once the TSs were located and characterized, subsequent minimum energy paths (MEPs) were traced down toward the corresponding minima, to ensure that the structures really connect reactants and intermediates. The reaction paths were obtained for both doublet and quartet spin state PESs from the corresponding TSs using a reaction coordinate (Rx) in a mass-weighted step of 0.01 amu$^{1/2}$ bohr. The calculations were performed at UB3LYP[26a,b]/LACVP*[26c] (consisting of the combination of the 6-31G(d) basis for all the atoms except for the iron one, which was represented by the

DOI: 10.1021/ct501030q
J. Chem. Theory Comput. 2015, 11, 1470−1480

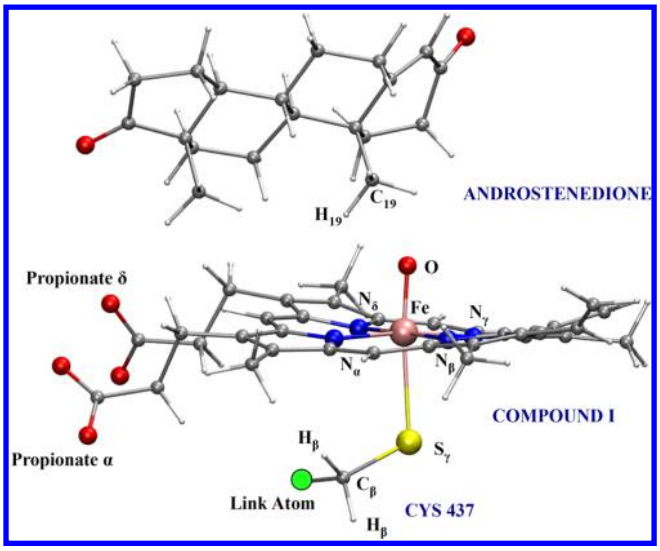

Figure 1. Atoms comprising the QM model: Cys-437, Compound I, and the substrate androstenedione.

LANL2DZ effective core potential) level. In addition, single point energy calculations for selected points along the MEP (50 points toward reactants and 50 toward intermediates) were carried out at the UB3LYP/6-31G(d) level, thus avoiding the use of pseudopotentials on the iron atom.

Finally, in order to check the effect of the enzymatic environment, calculations on an unpolarized gas-phase model were carried out. For this purpose, the same geometrical structures of the reaction paths were selected, and single point energy calculations were performed using the UB3LYP/6-31G(d) level, but without incorporating the enzymatic environment.

All the electronic calculations were performed using the Gaussian 03[27] family of programs, whereas the fDYNAMO[20] library was used for the molecular mechanics and MD simulations.

2.2. Evaluation of the Topological Analysis of the ELF and Thom's CT (BET Method). ELF and electron density analyses were performed at each point selected from the reaction path (100 points) by means of Dgrid-4.6 package[28] considering a rectangular parallelepiped grid with a step size of 0.1 bohr. The ELF basins were visualized using the Jmol[29] and VMD programs.[30]

The ELF function is a mathematical function that measures the likelihood of finding an electron in the neighborhood space of a reference electron located at a given point and with the same spin. This function takes numerical values mapped on the interval (0,1). Values close to 1 provide regions of the space where the probability of finding an electron pair in the molecular space is high. The topological analysis of the ELF gradient field[31] represents an alternative to the valence bond theory and molecular orbital approaches and provides the partition of the molecular space into basins of attractors that correspond to atomic cores, bonds, and lone pairs. The atomic cores coincide with the atomic nuclei and are labeled as C(A), being A the atomic symbol of the element. The concept of synapticity, introduced by Silvi et al.,[31b,32] allows the classification of η-localization basins in the ELF domain. In this way, it is possible to find monosynaptic basins, labeled as V(A), which correspond to lone pairs of the Lewis model, as well as disynaptic basins labeled as V(X,Y) which correspond with the ELF-localization basins with common surfaces between two C(X) and C(Y) core basins and are related to the chemical bonds. The mathematical branch that provides an appropriate framework to achieve the partition of the molecular space in regions related to the chemical properties is the theory of dynamical systems.[8b,33] A dynamical system is a mathematical model that describes the temporal evolution of the state of a physical system. The simplest model is the gradient dynamical system in which the gradient field of a scalar function provides the vector field.[34] For example, the differential equation of motion $\dot{x} = (dx/dt) = v(x)$ involves the time derivative of a trajectory on the phase space.

The elementary CT studies how the equilibria of a gradient system (or dynamical system) change as the control parameters change, by considering the behavior of the Hessian matrix (H_{ij}). According to this theory, the set of points at which the determinant of the Hessian matrix is nonzero, det $|H_{ij}| \neq 0$, are hyperbolic critical points; in contrast, the set of points at which the det $|H_{ij}| = 0$ are nonhyperbolic critical points or bifurcation points. The set of values for which the determinant of the Hessian matrix of a given critical point is nonzero defines the domain of stability of the critical point also known as structural stability domains (SSDs). When a small perturbation of the function (by means of changes in the control parameters) leads to a zero value of the determinant of the Hessian matrix (nonhyperbolic point), the system changes from one SSD to another through a bifurcation point (catastrophic point).

In a chemical reaction, the changes on the control parameters defining the reaction pathway (such as the nuclear coordinates and the electronic state) can lead to different topologies of the ELF. Along the reaction pathway, the chemical system goes from a given ELF-SSD to another by means of bifurcation catastrophes occurring at the turning points (TPs). In this way, a chemical reaction can be viewed as a dynamical system where a sequence of elementary chemical processes occur, being characterized by catastrophes. The bifurcation catastrophes occurring at these turning points may be identified according to Thom's classification. Only three types of bifurcation catastrophes have been found in chemical reactivity: (i) the fold catastrophe, corresponding to the creation or to the annihilation of two critical points of different parities; (ii) the cusp catastrophe, which transforms one critical point into three (and vice versa) such as in the formation or the breaking of a covalent bond; (iii) the elliptic umbilic, in which the index of a critical point changes by two. The characterization of the TPs connecting the ELF-SSDs along the reaction pathway allows us to catalog the different chemical events occurring during the course of the reaction as a sequence of electron pair rearrangements taking place during a chemical transformation.

3. RESULTS AND DISCUSSION

3.1. Energetic and Geometrical Parameters. The results presented in this paper correspond to the hydrogen abstraction from the substrate ASD by Cpd I in the active site of enzyme aromatase. In this reaction, a hydrogen abstraction process, that is also viewed as a case of hydrogen-atom transfer,[35] takes place from the C_{19} methyl of ASD to the ferryl (Fe═O) group of Cpd I, leading to the formation of the ASD alkyl radical intermediate as well as the iron−hydroxo complex.

The relative electrostatic potential energies (eq 1) obtained for the stationary points are shown in Table 1:

DOI: 10.1021/ct501030q
J. Chem. Theory Comput. 2015, 11, 1470−1480

$$E = E_{elec} = \langle \Psi | \hat{H}_0 | \Psi \rangle + \sum_{i}^{electrons} \sum_{m}^{MM\ atoms} \left\langle \Psi \left| \frac{q_m}{r_{i,m}} \right| \Psi \right\rangle \quad (1)$$

Table 1. Relative Electrostatic Potential Energies (ΔE, kcal/mol) for the Hydrogen Abstraction Process of Substrate ASD via Aromatase Enzyme Calculated at the UB3LYP/6-31G(d) Level[a,b]

		ΔE (kcal/mol)		
spin	electromer	R	TS	I
doublet	$^{2}Fe^{III}Por^{\bullet+}$	0.0	32.8	25.4
quartet	$^{4}Fe^{III}Por^{\bullet+}$	0.5	35.0	25.0
	$^{4}Fe^{IV}Por$		36.3	23.2

[a]The values correspond to the doublet and quartet spin state surfaces. The latter includes the energy of both electromeric situations found in the intermediate ($^{4}Fe^{III}Por^{\bullet+}$ and $^{4}Fe^{IV}Por$). [b]R, reactant; TS, transition state; I, intermediate.

The term $\langle \Psi | \hat{H}_0 | \Psi \rangle$ of eq 1 accounts for the selected gas-phase Hamiltonian ($\hat{H}_0$) operating on the polarized wave function (Ψ), while the second term corresponds to the electrostatic interaction of Ψ with the charges representing the atoms of the enzymatic environment (q_m) at a distance $r_{i,m}$. The MM charges that have been considered are those that are within 20 Å of Cpd I or the ASD substrate (a total of 8512 charges). It is worth noting that those terms corresponding to the MM potential of the total QM/MM energy have been neglected, since we are only interested in the electronic properties of the QM part. Thus, although the reaction paths obtained depend upon the Lennard-Jones interaction between the QM and MM regions, this classical contribution does not affect directly the wave function, and therefore it is important to remark that the results obtained from subsequent ELF based analysis are maintained.

As can be observed in Table 1 and Figure 2, the activation energy barriers for the enzymatic process are predicted to be 32.8 and 35.0 kcal/mol for the doublet and quartet, respectively. The slight difference between both values suggests that both states might be accessible during the reaction.

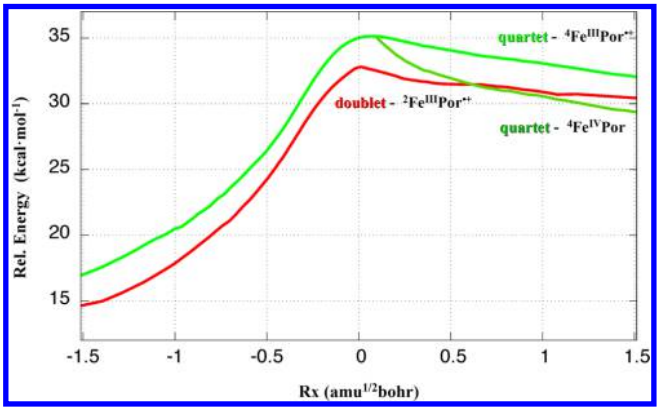

Figure 2. Potential energy profile corresponding to the hydrogen abstraction reaction from ASD in doublet and quartet spin states (reactant and intermediate species are not included). A bifurcation point on the quartet PES can be observed after the transition state, leading to the formation of two different electromers for the quartet state ($^{4}Fe^{III}Por^{\bullet+}$ and $^{4}Fe^{IV}Por$).

An analysis of Figure 2 shows the presence of a post-transition state bifurcation on the quartet state PES leading toward two different close-lying electromer intermediates that vary in the oxidation state of the iron center and the porphyrin ligand.[36]

According to the $^{2S+1}$**I**($Fe^{OS}Por$) nomenclature, four low-lying electronic states may be found ($^{2,4}Fe^{III}Por^{\bullet+}$ and $^{2,4}Fe^{IV}Por$) depending on the spin quantum number (S = 1/2, 3/2) and the oxidation states (OS = III, IV) on the iron center and the ligands.[37] In particular, only one electromeric situation was found for the doublet spin state ($^{2}Fe^{III}Por^{\bullet+}$) and two for the quartet state ($^{4}Fe^{III}Por^{\bullet+}$, $^{4}Fe^{IV}Por$) in the enzymatic system. In fact, this bifurcation corresponds to the crossing point of two different adiabatic surfaces for each electromeric distribution in the quartet state. In the present work we have eluded the initial part of the $^{4}Fe^{IV}Por$ reaction path previous to the crossing point, as long as it corresponds to a higher energy mechanistic profile.

On the other hand, the presence of electromers is not observed for gas-phase models. This can be attributed to the absence of specific interactions with the enzymatic environment[38] (mostly related to the sulfur axial ligand of the heme group). Therefore, a single energy profile has been obtained for each electronic state (doublet and quartet) when single point gas-phase calculations are performed along the enzymatic reaction paths (see Table S1 and Figure S1 of the Supporting Information).

The hydrogen abstraction process has been found to be endothermic with ΔE values of 25.4 kcal/mol for the doublet spin state, and 25.0 and 23.2 kcal/mol for the $^{4}Fe^{III}Por^{\bullet+}$ and $^{4}Fe^{IV}Por$ electromers, respectively. Likewise, after the system overcomes the transition state, the energy of the doublet lies between both quartet electromers, with $^{4}Fe^{IV}Por$ being about 2 kcal/mol more stable than $^{4}Fe^{III}Por^{\bullet+}$. Thus, the intermediate formed in this step brings about an alkyl radical on the C_{19} methyl of ASD as well as a hydroxyl group linked to the iron atom, and later gives rise to the oxygen rebound mechanism step.

The fact that the reported energies are too large for a chemical process catalyzed by an enzyme can be explained taking into account the following considerations: (i) These energies solely arise from the electronic terms of the hybrid QM/MM potential (see eq 1). (ii) The results are based merely on the PES analysis. In fact, the estimation of the Gibbs free energy of activation calculated with the 6-31G(d) basis set, by means of the total QM/MM potential energy and the rigid-rotor and harmonic-oscillator (RRHO) approximations applied to the ASD substrate, provides a lower activation barrier (25.5 kcal/mol) for the doublet process.

Furthermore, we have recently found that the free energy of activation for the hydrogen abstraction process, evaluated using free energy perturbation techniques, is about 13 kcal/mol, using the LACVP* basis set.[39] In the same study we determined that the major contributions to reducing the activation energy come from the polarization of the wave function and the Lennard-Jones potential; the electrostatic interaction is nonfavorable for the reaction in this particular chemical system.

All in all, it is not our intention to discuss in the present paper the role of cytochrome P450 aromatase as a biocatalyst, but to shed light on the different electronic rearrangements that take place during the hydrogen abstraction process carried out by this enzyme.

DOI: 10.1021/ct501030q
J. Chem. Theory Comput. 2015, 11, 1470−1480

Table 2. Atomic Spin Densities for Atoms or Fragments Included in the QM Model[a]

			TS		I	
fragment	spin	R	$Fe^{III}Por^{\bullet+}$	$Fe^{IV}Por$	$Fe^{III}Por^{\bullet+}$	$Fe^{IV}Por$
SCH_3^-	doublet	−0.19	−0.19		−0.16	
	quartet	0.17	0.13	−0.07	0.08	−0.07
Fe	doublet	1.39	1.13		1.03	
	quartet	1.32	1.06	2.03	0.96	2.10
O	doublet	0.73	0.46		0.10	
	quartet	0.74	0.50	0.46	0.12	0.11
Fe=O	doublet	2.12	1.59		1.14	
	quartet	2.06	1.56	2.48	1.09	2.21
C_{19}	doublet	0.00	0.57		1.01	
	quartet	0.00	0.59	0.68	1.03	1.02
H_{19}	doublet	0.00	−0.07		−0.00	
	quartet	0.00	−0.08	−0.04	−0.00	0.02
porphyrin	doublet	−0.93	−0.87		−0.95	
	quartet	0.76	0.81	−0.05	0.87	−0.11
substrate[b]	doublet	0.00	−0.02		−0.07	
	quartet	0.00	−0.02	−0.01	−0.06	−0.06

[a]The values are presented for both doublet and quartet spin states, with the latter including the two electromeric states found in the transition states and intermediate species ($Fe^{III}Por^{\bullet+}$ and $Fe^{IV}Por$). [b]Does not include the C_{19} and H_{19} atoms.

The Mulliken atomic spin densities obtained from single point calculations are reported in Table 2 (as well as in Table S2 of the Supporting Information for gas-phase calculations). These results reveal that two spin-up electrons are located on the FeO moiety (ρ(FeO) ∼ 2.10), forming a local triplet. A third electron is localized between the a_{2u} orbital of the porphyrin ring that leads to the A_{2u} electronic state and the π_s orbital of the Cys-437 sulfur atom leading to a Π_s electronic state. The sign of this unpaired spin density population (beta or alpha) determines either the doublet or quartet nature of the system, respectively. The results in Table 2 show a predominant A_{2u} state versus the Π_s state (with a ratio of ∼80%), in both doublet and quartet spin states, corresponding to a "green" Cpd I instead of the "red" one. As the reaction proceeds, the hydrogen H_{19} is transferred to the oxygen of Cpd I from the C_{19}, leading to the formation of a radical on this carbon ($\rho(C_{19})$ ∼ 1.00) and a hydroxyl group (ρ(OH) ∼ 0.10) linked to the iron atom. As discussed above, the iron−hydroxo complex has been found in two different electromeric configurations in the quartet spin state and only one in the doublet electronic state. The first electromer ($Fe^{III}Por^{\bullet+}$), containing one unpaired electron on the iron center and the other one distributed over the a_{2u} orbital and the sulfur atom, was found in both doublet (ρ(Fe) = 1.03, ρ(Por+SCH_3) = −1.08) and quartet states (ρ(Fe) = 0.96, ρ(Por+SCH_3) = 1.05). The second electromeric state ($Fe^{IV}Por$) containing the two unpaired electrons on the iron center (ρ(Fe) = 2.10 and ρ(Por+SCH_3) = −0.19) was only found in the quartet state, being 2 kcal/mol lower in energy than the other configuration. However, it is worth noting that all electromeric situations found retain the radical character on the C_{19} atom with a singly occupied orbital ($\rho(C_{19})$ = 1.01 ($^2Fe^{III}Por^{\bullet+}$), 1.03 ($^4Fe^{III}Por^{\bullet+}$), and 1.02 ($^4Fe^{IV}Por$)).

The most important geometrical parameters of the substrate and cofactor obtained during the hydrogen abstraction step are presented in Table 3. As can be noticed, the values obtained for both the Fe−S and Fe−O distances in the reactant species (R) are consistent with those observed experimentally for Cpd I[40] (2.48 and 1.65 Å respectively, using EXAFS spectroscopy). As the reaction proceeds, the Fe−O bond is stretched and there is

Table 3. Selected Geometrical Parameters[a]

	doublet			quartet		
	R	TS	I	R	TS	I
Fe−S	2.681	2.588	2.527	2.659	2.564	2.488
Fe−O	1.625	1.761	1.801	1.626	1.761	1.802
O−C_{19}	2.907	2.525	2.895	2.906	2.518	2.871
C_{19}−H_{19}	1.091	1.399	2.044	1.092	1.394	2.182
O−H_{19}	2.487	1.133	0.976	2.383	1.134	0.974
S−Fe−O	173.9	170.2	172.4	173.6	170.2	172.8
C_{19}−H_{19}−O	101.5	171.2	144.5	107.6	169.6	126.6

[a]Distances are in angstroms, and angles are in degrees.

a shortening in the bond length between the iron atom and the sulfur axial ligand due to the formation of the new hydroxyl group (d(O−H_{19}) = 0.976 Å). Moreover, the C_{19}−H_{19}−O angle shows its maximum value close to the linearity (∼170°) at the transition structure of the hydrogen abstraction step, as expected for this kind of reaction.

3.2. Topological Analysis. The basin populations along the MEP pathway are summarized in Tables 4, 5, and 6. For convenience, only basin populations directly related to the rearrangements of the C_{19}−H_{19} and O−H_{19} bonds have been considered for discussion. Moreover, due to the valence shell compactness of the O atom, the overall population of its monosynaptic basins (V_u(O)) has been considered instead of their internal reorganizations, thus focusing on those ELF topological changes which are more relevant for the hydrogen abstraction. Likewise, the specific monosynaptic basin found surrounding the C(O) core basin region on the line joining the H_{19} and O nuclei, labeled V_x(O), has been treated apart from the rest of V_u(O) monosynaptic basins, as long as it would be directly related to the radical character of the ferryl moiety (FeO). Finally, the reaction coordinates have been traced from −9.8 to 6.9 $amu^{1/2}$ bohr for the doublet and from −10.7 to 8.9 $amu^{1/2}$ bohr for the quartet.

The MEP of the hydrogen abstraction step is reported in Figure 3 together with the different ELF topologies along the reaction coordinate (also, a video animation is available in the Supporting Information). In terms of the ELF topological

DOI: 10.1021/ct501030q
J. Chem. Theory Comput. 2015, 11, 1470−1480

Table 4. Population of the Most Significant Basins Involved in the Hydrogen Abstraction Reaction in Doublet Spin State[a]

	SSD-I		SSD-II		SSD-III			SSD-IV		SSD-V	
basin	reactant	last point	first point	last point	first point	TS	last point	first point	last point	first point	intermediate
$V(C_{18},C_{19})$	1.85	1.86	1.86	1.85	1.85	1.82	1.78	1.78	1.75	1.75	1.66
$V(C_{19},H_{17})$	2.01	2.03	2.03	2.04	2.04	2.06	2.07	2.07	2.01	2.01	1.84
$V(C_{19},H_{18})$	2.00	2.02	2.02	2.03	2.03	2.05	2.09	2.10	2.22	2.02	1.80
$V(C_{19},H_{19})$	2.01	2.01	2.01	2.01							
$V_1(C_{19})$					1.29	1.60	1.69	1.69	1.69	1.69	1.41
$V_2(C_{19})$										0.20	1.07
$V(H_{19})$					0.71	0.51	0.59				
$V_u(O)$	7.38	7.29	6.92	6.95	6.98	6.34	6.14	6.13	6.07	6.07	5.97
$V_x(O)$			0.38	0.34	0.29	0.87	0.94				
$V(O,H_{19})$								1.53	1.57	1.57	1.60
Rx ($amu^{1/2}$ bohr)	−9.841	−0.527	−0.489	−0.323	−0.304	0.000	0.262	0.280	0.947	0.966	6.947
energy (kcal/mol)	0.00	23.78	24.44	27.90	28.34	32.77	31.88	31.83	31.01	30.97	25.39

[a]The anterior and posterior points to the turning points as well as the stationary points are also included.

Table 5. Population of the Most Significant Basins Involved in the Hydrogen Abstraction Reaction in Quartet Spin State, for the $^4Fe^{III}Por^{\bullet+}$ Electromer[a]

	SSD-I		SSD-II		SSD-III			SSD-IV		SSD-V	
basin	reactant	last point	first point	last point	first point	TS	last point	first point	last point	first point	intermediate
$V(C_{18},C_{19})$	1.85	1.86	1.84	1.86	1.84	1.85	1.77	1.76	1.74	1.75	1.68
$V(C_{19},H_{17})$	2.01	2.04	2.04	2.04	2.04	2.06	2.06	2.06	1.99	1.99	1.85
$V(C_{19},H_{18})$	2.01	2.02	2.02	2.02	2.02	2.04	2.09	2.09	2.23	2.03	1.81
$V(C_{19},H_{19})$	2.00	1.96	2.06	1.95							
$V_1(C_{19})$					1.42	1.43	1.76	1.75	1.73	1.73	1.30
$V_2(C_{19})$										0.20	1.09
$V(H_{19})$					0.66	0.54	0.59				
$V_u(O)$	7.40	7.03	6.68	6.66	6.66	6.53	6.05	6.04	5.99	5.99	5.82
$V_x(O)$			0.63	0.60	0.65	0.61	1.00				
$V(O,H_{19})$								1.59	1.61	1.61	1.61
Rx ($amu^{1/2}$ bohr)	−10.787	−0.321	−0.302	−0.284	−0.265	0.000	0.246	0.265	0.631	0.652	8.935
energy (kcal/mol)	0.54	30.13	30.56	30.97	31.39	35.02	34.75	34.69	33.73	33.69	25.03

[a]The anterior and posterior points to the turning points as well as the stationary points are also included.

Table 6. Population of the Most Significant Basins Involved in the Hydrogen Abstraction Reaction in Quartet Spin State, for the $^4Fe^{IV}Por$ Electromer[a]

	SSD-I		SSD-II		SSD-III			SSD-IV		SSD-V	
basin	reactant	last point	first point	last point	first point	TS	last point	first point	last point	first point	intermediate
$V(C_{18},C_{19})$	1.85	1.86	1.84	1.86	1.84	1.85	1.82	1.82	1.78	1.77	1.73
$V(C_{19},H_{17})$	2.01	2.04	2.04	2.04	2.04	2.06	2.07	2.07	2.04	2.02	1.92
$V(C_{19},H_{18})$	2.01	2.02	2.02	2.02	2.02	2.04	2.07	2.07	2.22	2.05	1.87
$V(C_{19},H_{19})$	2.00	1.96	2.06	1.95							
$V_1(C_{19})$					1.42	1.43	1.53	1.53	1.53	1.53	1.14
$V_2(C_{19})$										0.20	0.95
$V(H_{19})$					0.66	0.54	0.60				
$V_u(O)$	7.40	7.03	6.68	6.66	6.66	6.53	6.26	6.24	6.06	6.06	5.92
$V_x(O)$			0.63	0.60	0.65	0.61	0.78				
$V(O,H_{19})$								1.39	1.53	1.54	1.60
Rx ($amu^{1/2}$ bohr)	−10.787	−0.321	−0.302	−0.284	−0.265	0.000	0.189	0.208	1.120	1.174	8.935
energy (kcal/mol)	0.54	30.13	30.56	30.97	31.39	36.33	33.90	33.69	30.26	30.12	23.15

[a]The anterior and posterior points to the turning points as well as the stationary points are also included.

description, the C−H breaking and the subsequent O−H bond formation has been found to take place in five ELF-SSDs, which are connected by their respective turning points. This topological response has been found both in low and high spin configurations. The ELF evolution along the MEP displays in both spin configurations a certain synchronicity: (i) SSD-I and SSD-II have been localized before the respective transition states; (ii) the TSs are localized on the SSD-III; (iii) SSD-IV and SSD-V have been found after the TS.

In Figure 4, the evolution of valence attractors obtained from the ELF gradient field along the reaction path is schematically displayed. At the beginning of the process the $V(C_{19},H_{19})$ basin

DOI: 10.1021/ct501030q
J. Chem. Theory Comput. 2015, 11, 1470−1480

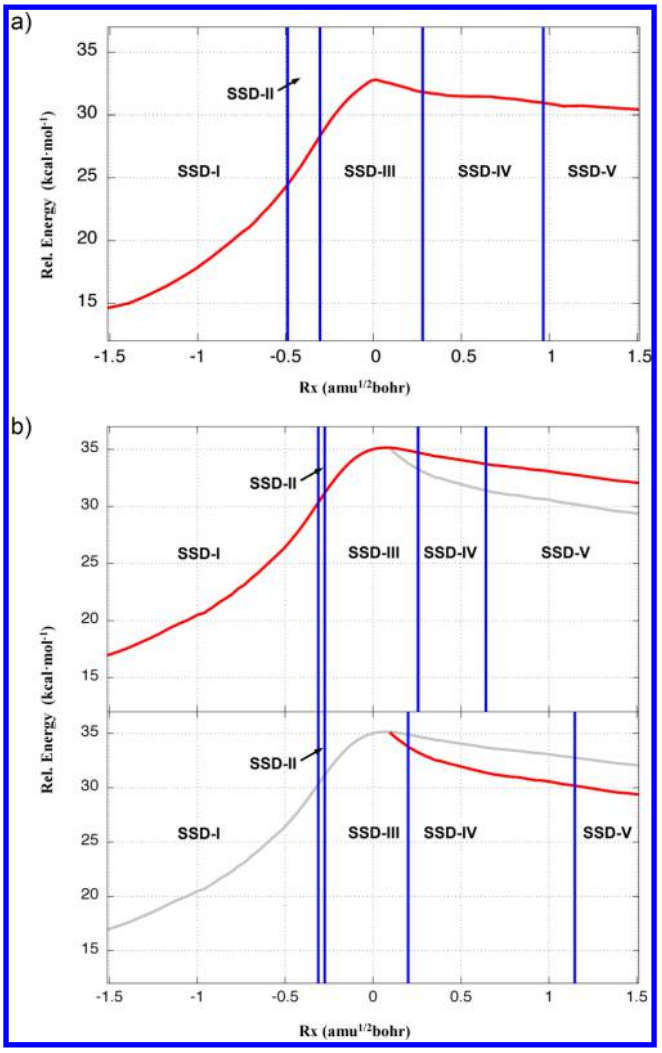

Figure 3. MEP of the hydrogen abstraction reaction in doublet and quartet spin states with marked SSDs obtained from BET analysis. (a) MEP path for the doublet spin. (b) MEP path for both electromeric states obtained for the quartet spin. The top image shows the $^4Fe^{III}Por^{\bullet+}$ electromer, while the bottom image shows $^4Fe^{IV}Por$ electromer.

populations are calculated to be 2.00 e for the doublet and the quartet, while the overall $V_u(O)$ basin populations are predicted to be 7.38 and 7.40, respectively. In this way, the first topological change is predicted to be at ≈ -0.49 amu$^{1/2}$ bohr (doublet) and ≈ -0.30 amu$^{1/2}$ bohr (quartet) connecting the SDD-I and SSD-II, which is associated with the creation of the $V_x(O)$ monosynaptic basin and a fold-type of catastrophe. The $V_x(O)$ basin population has been predicted to be 0.38 e and 0.63 e for the doublet and the quartet, respectively. It is worth noting that the energetic cost associated with SSD-I and SSD-II not only comprises the energetic cost associated with electronic density rearrangement anticipating the breaking process of the $C_{19}-H_{19}$ bond, it also involves the rotation of the methyl group allowing the closest orientation between the H_{19} and O atoms. Later, the second topological change connecting SSD-II and SSD-III has been predicted at ≈ -0.30 amu$^{1/2}$ bohr (doublet) and ≈ -0.26 amu$^{1/2}$ bohr (quartet). This topological change represents thus a cusp type of catastrophe associated with the breaking process of the $C_{19}-H_{19}$ bond, where the $V(C_{19},H_{19})$ disynaptic basin splits into two monosynaptic basins, namely, $V(H_{19})$ and $V(C_{19})$; see Figure 4. The respective basin populations for these monosynaptic basins are predicted to be 0.71 e and 1.29 e for the doublet and 0.66 e and 1.42 e for the quartet, respectively. Despite this topological change, the nearby $V(C_{19},C_{18})$, $V(C_{19},H_{18})$, and $V(C_{19},H_{17})$ basin populations which belong to the ASD moiety do not seem to be affected by the sudden topological change of the ELF field (see Tables 4−6). However, when the system reaches the transition state, the radical character of the C_{19} and O atoms enhances; their respective basin populations increase up to 1.60 e and 1.43 e for $V(C_{19})$ and up to 0.87 e and 0.61 e for the $V_x(O)$ in low and high spin configurations, respectively. In contrast the $V(H_{19})$ basin population decreases up to 0.51 e and 0.54 e, for low and high spin configurations, respectively. Interestingly, from an ELF-topological point of view, when the system reaches the transition state there is no evidence of the formation of the $O-H_{19}$ bond. Subsequently, when the system overcomes the transition state, and then reaches the end of the SSD-III, a considerable increase in the $V_x(O)$ basin population is observed in both spin configurations (around $\approx$1.0 e). Likewise, the $V(H_{19})$ basin population increases its value up to 0.60 e in both electronic states. The role of the SSD-III is therefore to prepare the system for the imminent formation of the $O-H_{19}$ bond, while the energy increases by $\approx$4.4/3.6 kcal/mol (doublet and quartet) until the TS is reached.

Afterward, a new turning point connecting SSD-III and SSD-IV is found. For the low spin configuration it is localized at $\approx$0.28 amu$^{1/2}$ bohr, whereas for the quartet state the corresponding turning points of each electromer are localized at 0.26 and 0.21 amu$^{1/2}$ bohr. The nonbonding monosynaptic attractors $V(H_{19})$ and $V_x(O)$ are replaced by a single bonding disynaptic attractor $V(O,H_{19})$, which corresponds to a cusp type of catastrophe. Thus, from an ELF-topological point of view, this is the first evidence of the formation of the O−H

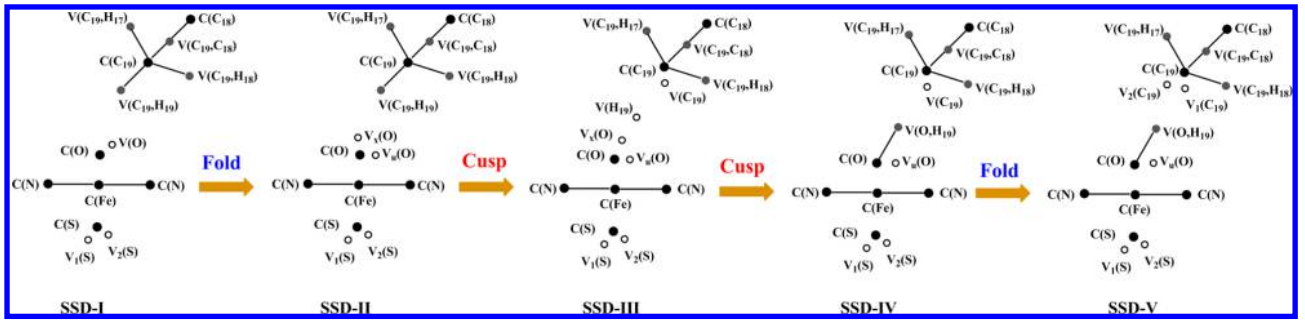

Figure 4. Evolution of valence attractors obtained from ELF gradient field along the reaction path. The respective types of catastrophes are indicated. Black balls correspond to core basins, and gray balls correspond to valence basins.

DOI: 10.1021/ct501030q
J. Chem. Theory Comput. 2015, 11, 1470−1480

bond, which in turn takes place after overcoming the transition state. On the first point of the SSD-IV, the $V(O,H_{19})$ basin populations are predicted to be 1.53 e for the doublet, and 1.59 e and 1.39 e for the respective quartet electomers. Likewise, the $V(C_{19})$ basin populations are calculated to be 1.69 e for the doublet, and 1.75 e and 1.53 e for the quartet. Subsequently, during the progress of the SSD-IV, the $V(C_{19})$ monosynaptic basin populations remain practically constant while the populations of the $V(C_{19},H_{18})$ disynaptic basin increases. This fact indicates that along the SSD-IV a partial charge density is concentrated on the $V(C_{19},H_{18})$ disynaptic basin rather than $V(C_{19})$. As shown in previous articles,[41] a basin population larger than ≈2.00 e for a C−H bond suggests that it can hide a partial charge density of the monosynaptic basin V(C), corresponding to an unpaired electron on the C atom, overlapped by the hydrogenated basin. Therefore, during the progress of the SSD-IV the electronic flux is directed toward the C_{19} atom, increasing the radical character of this atom.

Finally, when the system reaches the last turning point connecting SSD-IV and SSD-V, a fold-type of catastrophe is localized at ≈0.97 $amu^{1/2}$ bohr for the doublet, and 0.65 and 1.17 $amu^{1/2}$ bohr for the respective quartet electromers. It is worth noting that the SSD-V found in the $^4Fe^{IV}Por$ electromer is delayed along the reaction path with respect to the $^4Fe^{III}Por^{\bullet+}$ electromer; this fact is consistent with the different electronic structures of both electromers. In this turning point a new $V_2(C_{19})$ monosynaptic attractor is created due to an excess of the charge density around the C_{19} atom indicating a permanent electronic flow toward this atom from the $V_1(C_{19})$ monosynaptic basin as well as from the $V(C_{19},H_{17})$ and $V(C_{19},H_{18})$ disynaptic basins. Thus, when the system reaches the radical intermediate, the basin population for $V_2(C_{19})$ has increased up to 1.07 e at low spin configuration, whereas for the quartet state these values have been predicted to be 1.09 e and 0.95 e for the respective $^4Fe^{III}Por^{\bullet+}$ and $^4Fe^{IV}Por$ electromers (see Tables 4, 5 and 6).

On the other hand, the results obtained once the BET analysis was performed in the gas phase (single point energy calculations) show results similar to those in the enzymatic system. In this way, the same number and type of stability domains (SSD-I−SSD-V) are found in the gas-phase model, being characterized by the same type of catastrophes. Furthermore, the populations for the different basins obtained with the ELF analysis in both spin states give rise to virtually the same values for either the gas-phase model or the enzymatic system (see Tables S3 and S4 and Figure S1 of the Supporting Information). The only difference between these models lies in that these catastrophes appear in different values of the reaction coordinate, showing that electronic rearrangement occurs slightly differently in the enzyme and gas phase (see Figures S2 and S3 in the Supporting Information). In particular, it can be shown that the last turning point that connects the SSD-IV and SSD-V through a fold-type catastrophe is found at lower values along the reaction coordinate for the gas-phase model than in the enzymatic system (0.76 and 0.54 $amu^{1/2}$ bohr for the doublet and the quartet respectively in the gas-phase model). These findings also show that the quartet state in the gas-phase model is more similar to the $^4Fe^{III}Por^{\bullet+}$ electromer (0.65 $amu^{1/2}$ bohr) than to the $^4Fe^{IV}Por$ one (1.17 $amu^{1/2}$ bohr). However, the two first turning points that give rise to the stability domains from SSD-I to SSD-III take place in similar values of the reaction coordinate in both the enzymatic and gas-phase models. Since those SSDs are involved in the activation of the C−H bond, this suggests that the electronic process that takes place during the C−H bond activation is minimally affected by the electrostatic environment of the enzyme.

4. CONCLUSIONS

In summary, from the results of the present work, we can drawn the following conclusions:

(i) In this article we have introduced a novel approach to analyze the progress of a biochemical reaction taking into account an inhomogeneous enzymatic environment. We have demonstrated the applicability of BET coupled with QM/MM methods as a useful and powerful tool to study complex enzymatic reactions involving large biological systems. This is the first study where the combination of both methods has been applied to study the hydrogen abstraction process catalyzed by P450. We are able to describe the electronic reorganization, how the electrons flow along the reaction progress, and when and how the bond breaking/forming processes and/or electron pair rearrangements take place.

(ii) Chemical events provided by BET allows us to characterize five different SSDs for the hydrogen abstraction process. Thus, the hydrogen abstraction step is found to be a nonconcerted process, inasmuch as the C−H bond breaking and the O−H bond formation processes do not take place at the same time. As a result, the reaction pathway associated with the hydrogen abstraction process first involves a methyl rotation, then the breaking process of the C−H bond, and finally the formation of the O−H bond, localized after the transition state.

(iii) The presence of electromers in the high spin (quartet) configuration obtained in the enzymatic system (not in the gas-phase model) has been found; however, these electromers do not affect the evolution of the ELF field along the reaction coordinate. Both electromers give rise to the same radical intermediate; nevertheless the SSD-V appears slightly delayed for the $^4Fe^{IV}Por$ electromer.

(iv) When comparing the results provided by the BET in the enzyme system and in the gas-phase model, it has been observed that the same domains (SSD-I − SSD-V) are found in both models, which are characterized by the same type of catastrophes. The only difference between these models lies in the different values of the reaction coordinate at which these catastrophes take place. This difference, which is not large, shows that electronic rearrangement occurs slightly differently in the enzyme and in the gas phase, suggesting that the chemical reaction is almost electronically equivalent in both models. Based on these findings, we can conclude that this cytochrome may provide different sources of stabilization than the electrostatic contribution, and may increase the degree of electronic diversity of the heme group, i.e., the presence of electromers.

We believe that the general approach presented here can be further extended to study an even wider range of biological systems. Moving forward, a number of extensions of the present method should be explored, in particular in enzyme catalysis that are currently underway within our group.

■ ASSOCIATED CONTENT

Supporting Information

Energies, spin densities, and populations of the most significant basins obtained from single point energy calculations in gas-phase are reported. Video animations of the different ELF topologies along the reaction coordinate, showing the different

DOI: 10.1021/ct501030q
J. Chem. Theory Comput. 2015, 11, 1470−1480

SSDs, are available for both the doublet and quartet states. This material is available free of charge via the Internet at http://pubs.acs.org.

AUTHOR INFORMATION

Corresponding Author

*E-mail: andres@uji.es.

Funding

This work was supported by MINECO Projects CTQ2012-36253-C03-01 and CTQ2012-36253-C03-02, by Prometeo/2009/053 and Prometeo/2014/022 (Generalitat Valenciana), and by BANCAIXA Project P1.1B2011-23. I.V. thanks the Spanish Ministerio de Ciencia e Innovación for a doctoral grant (CTQ2009-14541-C02).

Notes

The authors declare no competing financial interest.

ACKNOWLEDGMENTS

We acknowledge the Servei d'Informàtica of the Universitat Jaume I.

REFERENCES

(1) Bader, R. F. W. *Atoms in Molecules: A Quantum Theory*; Oxford University Press: Oxford, 1990; p *xviii*, 438 pp.

(2) Becke, A. D.; Edgecombe, K. E. A simple measure of electron localization in atomic and molecular systems. *J. Chem. Phys.* **1990**, *92* (9), 5397−5403.

(3) Chesnut, D. B. An Electron Localization Function Study of the Lone Pair. *J. Phys. Chem. A* **2000**, *104* (49), 11644−11650.

(4) (a) Nesper, R. Bonding Patterns in Intermetallic Compounds. *Angew. Chem., Int. Ed. Engl.* **1991**, *30* (7), 789−817. (b) Savin, A.; Nesper, R.; Wengert, S.; Fässler, T. F. ELF: The Electron Localization Function. *Angew. Chem., Int. Ed. Engl.* **1997**, *36* (17), 1808−1832.

(5) (a) Popelier, P. L. A. Quantum Chemical Topology: on Bonds and Potentials. In *Intermolecular Forces and Clusters*; Wales, D. J., Ed.; Springer-Verlag: Berlin, 2005; Vol. *115*, pp 1−56. (b) Popelier, P. L. A.; Aicken, F. M.; O'Brien, S. E. Atoms in molecules. In *Chemical Modelling: Applications and Theory*, Hinchliffe, A., Ed.; The Royal Society of Chemistry: Cambridge, U.K., 2000; Vol. *1*, pp 143−198. (c) Popelier, P. L. A.; Smith, P. J. Quantum topological atoms. In *Chemical Modelling: Applications and Theory*; Hinchliffe, A., Ed.; The Royal Society of Chemistry: Cambridge, U.K., 2002; Vol. *2*, pp 391−448. (d) Malcolm, N. O. J.; Popelier, P. L. A. The full topology of the Laplacian of the electron density: scrutinising a physical basis for the VSEPR model. *Faraday Discuss.* **2003**, *124*, 353−363.

(6) (a) Warshel, A.; Levitt, M. Theoretical studies of enzymic reactions: Dielectric, electrostatic and steric stabilization of the carbonium ion in the reaction of lysozyme. *J. Mol. Biol.* **1976**, *103* (2), 227−249. (b) Singh, U. C.; Kollman, P. A. A combined ab initio quantum mechanical and molecular mechanical method for carrying out simulations on complex molecular systems: Applications to the CH3Cl + Cl− exchange reaction and gas phase protonation of polyethers. *J. Comput. Chem.* **1986**, *7* (6), 718−730. (c) Field, M. J.; Bash, P. A.; Karplus, M. A combined quantum mechanical and molecular mechanical potential for molecular dynamics simulations. *J. Comput. Chem.* **1990**, *11* (6), 700−733. (d) Senn, H. M.; Thiel, W. QM/MM Methods for Biomolecular Systems. *Angew. Chem., Int. Ed.* **2009**, *48* (7), 1198−1229. (e) Lonsdale, R.; Ranaghan, K. E.; Mulholland, A. J. Computational enzymology. *Chem. Commun.* **2010**, *46* (14), 2354−2372. (f) Ferrer, S.; Ruiz-Pernía, J.; Martí, S.; Moliner, V.; Tuñón, I.; Bertrán, J.; Andrés, J. Hybrid Schemes Based on Quantum Mechanics/Molecular Mechanics Simulations: Goals to Success, Problems, and Perspectives. In *Advances in Protein Chemistry and Structural Biology*; Christo, C., Ed.; Academic Press: San Diego, CA, USA, 2011; Vol. *85*, pp 81−142. (g) Sousa, S. F.; Fernandes, P. A.; Ramos, M. J. Computational enzymatic catalysis—clarifying enzymatic mechanisms with the help of computers. *Phys. Chem. Chem. Phys.* **2012**, *14* (36), 12431−12441.

(7) (a) Fang, D.; Chaudret, R.; Piquemal, J.-P.; Cisneros, G. A. Toward a Deeper Understanding of Enzyme Reactions Using the Coupled ELF/NCI Analysis: Application to DNA Repair Enzymes. *J. Chem. Theory Comput.* **2013**, *9* (5), 2156−2160. (b) Chaudret, R.; Piquemal, J.-P.; Cisneros, G. A. Correlation between electron localization and metal ion mutagenicity in DNA synthesis from QM/MM calculations. *Phys. Chem. Chem. Phys.* **2011**, *13* (23), 11239−11247. (c) Fang, D.; Lord, R. L.; Cisneros, G. A. Ab Initio QM/MM Calculations Show an Intersystem Crossing in the Hydrogen Abstraction Step in Dealkylation Catalyzed by AlkB. *J. Phys. Chem. B* **2013**, *117* (21), 6410−6420.

(8) (a) Krokidis, X.; Noury, S.; Silvi, B. Characterization of Elementary Chemical Processes by Catastrophe Theory. *J. Phys. Chem. A* **1997**, *101* (39), 7277−7282. (b) Thom, R. *Structural Stability and Morphogenesis; An Outline of a General Theory of Models*; W. A. Benjamin: Reading, MA, USA, 1975.

(9) (a) Andres, J.; Berski, S.; Domingo, L. R.; Polo, V.; Silvi, B. Describing the Molecular Mechanism of Organic Reactions by Using Topological Analysis of Electronic Localization Function. *Curr. Org. Chem.* **2011**, *15* (20), 3566−3575. (b) Andrés, J.; González-Navarrete, P.; Safont, V. S. Unraveling reaction mechanisms by means of Quantum Chemical Topology Analysis. *Int. J. Quantum Chem.* **2014**, *114* (19), 1239−1252. (c) Polo, V.; Andres, J.; Berski, S.; Domingo, L. R.; Silvi, B. Understanding Reaction Mechanisms in Organic Chemistry from Catastrophe Theory Applied to the Electron Localization Function Topology. *J. Phys. Chem. A* **2008**, *112* (31), 7128−7136. (d) Gillet, N.; Chaudret, R.; Contreras-García, J.; Yang, W.; Silvi, B.; Piquemal, J.-P. Coupling Quantum Interpretative Techniques: Another Look at Chemical Mechanisms in Organic Reactions. *J. Chem. Theory Comput.* **2012**, *8* (11), 3993−3997. (e) Andrés, J.; Gracia, L.; González-Navarrete, P.; Safont, V. S. Chemical structure and reactivity by means of quantum chemical topology analysis. *Comput. Theor. Chem.* **2015**, *1053*, 15−17.

(10) (a) Simpson, E. R.; Mahendroo, M. S.; Means, G. D.; Kilgore, M. W.; Hinshelwood, M. M.; Graham-Lorence, S.; Amarneh, B.; Ito, Y. J.; Fisher, C. R.; Michael, M. D.; Mendelson, C. R.; Bulun, S. E. Aromatase cytochrome P450, the enzyme responsible for estrogen biosynthesis. *Endocr. Rev.* **1994**, *15* (3), 342−355. (b) Ghosh, D.; Griswold, J.; Erman, M.; Pangborn, W. X-ray structure of human aromatase reveals an androgen-specific active site. *J. Steroid Biochem. Mol. Biol.* **2010**, *118* (4−5), 197−202.

(11) (a) Santen, R. J.; Brodie, H.; Simpson, E. R.; Siiteri, P. K.; Brodie, A. History of Aromatase: Saga of an Important Biological Mediator and Therapeutic Target. *Endocr. Rev.* **2009**, *30* (4), 343−375. (b) Brueggemeier, R. W.; Hackett, J. C.; Diaz-Cruz, E. S. Aromatase inhibitors in the treatment of breast cancer. *Endocr. Rev.* **2005**, *26* (3), 331−345.

(12) Hong, Y.; Cho, M.; Yuan, Y. C.; Chen, S. Molecular basis for the interaction of four different classes of substrates and inhibitors with human aromatase. *Biochem. Pharmacol.* **2008**, *75* (5), 1161−1169.

(13) Ortiz de Montellano, P. R. *Cytochrome P450 Structure, Mechanism, and Biochemistry*, 3rd ed.; Kluwer Academic/Plenum Publishers: New York, NY, USA, 2005.

(14) (a) Groves, J. T.; McClusky, G. A. Aliphatic hydroxylation via oxygen rebound. Oxygen transfer catalyzed by iron. *J. Am. Chem. Soc.* **1976**, *98* (3), 859−861. (b) Groves, J. T. Key elements of the chemistry of cytochrome P-450: The oxygen rebound mechanism. *J. Chem. Educ.* **1985**, *62* (11), 928−931. (c) Filatov, M.; Harris, N.; Shaik, S. On the "rebound" mechanism of alkane hydroxylation by cytochrome P450: Electronic structure of the intermediate and the electron transfer character in the rebound step. *Angew. Chem., Int. Ed.* **1999**, *38* (23), 3510−3512.

(15) Viciano, I.; Berski, S.; Martí, S.; Andrés, J. New insight into the electronic structure of iron(IV)-oxo porphyrin compound I. A quantum chemical topological analysis. *J. Comput. Chem.* **2013**, *34* (9), 780−789.

DOI: 10.1021/ct501030q
J. Chem. Theory Comput. 2015, 11, 1470−1480

(16) Shaik, S.; de Visser, S. P.; Ogliaro, F.; Schwarz, H.; Schroder, D. Two-state reactivity mechanisms of hydroxylation and epoxidation by cytochrome P-450 revealed by theory. *Curr. Opin. Chem. Biol.* **2002**, *6* (5), 556−567.
(17) Schröder, D.; Shaik, S.; Schwarz, H. Two-State Reactivity as a New Concept in Organometallic Chemistry. *Acc. Chem. Res.* **2000**, *33* (3), 139−145.
(18) Ghosh, D.; Griswold, J.; Erman, M.; Pangborn, W. Structural basis for androgen specificity and oestrogen synthesis in human aromatase. *Nature* **2009**, *457* (7226), 219−223.
(19) Li, H.; Robertson, A. D.; Jensen, J. H. Very fast empirical prediction and rationalization of protein pKa values. *Proteins: Struct., Funct., Bioinf.* **2005**, *61* (4), 704−721.
(20) Field, M. J.; Albe, M.; Bret, C.; Proust-De Martin, F.; Thomas, A. The dynamo library for molecular simulations using hybrid quantum mechanical and molecular mechanical potentials. *J. Comput. Chem.* **2000**, *21* (12), 1088−1100.
(21) Dewar, M. J. S.; Zoebisch, E. G.; Healy, E. F.; Stewart, J. J. P. Development and use of quantum mechanical molecular models. 76. AM1: a new general purpose quantum mechanical molecular model. *J. Am. Chem. Soc.* **1985**, *107* (13), 3902−3909.
(22) Jorgensen, W. L.; Maxwell, D. S.; Tirado-Rives, J. Development and Testing of the OPLS All-Atom Force Field on Conformational Energetics and Properties of Organic Liquids. *J. Am. Chem. Soc.* **1996**, *118* (45), 11225−11236.
(23) Jorgensen, W. L.; Chandrasekhar, J.; Madura, J. D.; Impey, R. W.; Klein, M. L. Comparison of simple potential functions for simulating liquid water. *J. Chem. Phys.* **1983**, *79* (2), 926−935.
(24) (a) Martí, S.; Moliner, V.; Tunon, I. Improving the QM/MM description of chemical processes: A dual level strategy to explore the potential energy surface in very large systems. *J. Chem. Theory Comput.* **2005**, *1* (5), 1008−1016. (b) Zhang, Y. K.; Liu, H. Y.; Yang, W. T. Free energy calculation on enzyme reactions with an efficient iterative procedure to determine minimum energy paths on a combined ab initio QM/MM potential energy surface. *J. Chem. Phys.* **2000**, *112* (8), 3483−3492.
(25) (a) Baker, J. Constrained optimization in delocalized internal coordinates. *J. Comput. Chem.* **1997**, *18* (8), 1079−1095. (b) Baker, J.; Kessi, A.; Delley, B. The generation and use of delocalized internal coordinates in geometry optimization. *J. Chem. Phys.* **1996**, *105* (1), 192−212. (c) Byrd, R. H.; Lu, P.; Nocedal, J.; Zhu, C. A Limited Memory Algorithm for Bound Constrained Optimization. *SIAM J. Sci. Comput.* **1995**, *16* (5), 1190−1208.
(26) (a) Lee, C.; Yang, W.; Parr, R. G. Development of the Colle-Salvetti correlation-energy formula into a functional of the electron density. *Phys. Rev. B* **1988**, *37* (2), 785−789. (b) Becke, A. D. Density-functional thermochemistry. III. The role of exact exchange. *J. Chem. Phys.* **1993**, *98* (7), 5648−5652. (c) Hay, P. J.; Wadt, W. R. Ab initio effective core potentials for molecular calculations. Potentials for K to Au including the outermost core orbitals. *J. Chem. Phys.* **1985**, *82* (1), 299−310.
(27) Frisch, M. J.; Trucks, G. W.; Schlegel, H. B.; Scuseria, G. E.; Robb, M. A.; Cheeseman, J. R.; Montgomery, J. A., Jr.; Vreven, T.; Kudin, K. N.; Burant, J. C.; Millam, J. M.; Iyengar, S. S.; Tomasi, J.; Barone, V.; Mennucci, B.; Cossi, M.; Scalmani, G.; Rega, N.; Petersson, G. A.; Nakatsuji, H.; Hada, M.; Ehara, M.; Toyota, K.; Fukuda, R.; Hasegawa, J.; Ishida, M.; Nakajima, T.; Honda, Y.; Kitao, O.; Nakai, H.; Klene, M.; Li, X.; Knox, J. E.; Hratchian, H. P.; Cross, J. B.; Bakken, V.; Adamo, C.; Jaramillo, J.; Gomperts, R.; Stratmann, R. E.; Yazyev, O.; Austin, A. J.; Cammi, R.; Pomelli, C.; Ochterski, J. W.; Ayala, P. Y.; Morokuma, K.; Voth, G. A.; Salvador, P.; Dannenberg, J. J.; Zakrzewski, V. G.; Dapprich, S.; Daniels, A. D.; Strain, M. C.; Farkas, O.; Malick, D. K.; Rabuck, A. D.; Raghavachari, K.; Foresman, J. B.; Ortiz, J. V.; Cui, Q.; Baboul, A. G.; Clifford, S.; Cioslowski, J.; Stefanov, B. B.; Liu, G.; Liashenko, A.; Piskorz, P.; Komaromi, I.; Martin, R. L.; Fox, D. J.; Keith, T.; Al-Laham, M. A.; Peng, C. Y.; Nanayakkara, A.; Challacombe, M.; Gill, P. M. W.; Johnson, B.; Chen, W.; Wong, M. W.; Gonzalez, C.; Pople, J. A. *Gaussian 03*, revision D.02; Gaussian, Inc.: Wallingford, CT, USA, 2004.
(28) Kohout, M. *DGrid*, version 4.6; Radebeul, Germany, 2011.
(29) Jmol: an open-source Java viewer for chemical structures in 3D. *Jmol*, version 14.2.7; SourceForge, Inc.: Mountain View, CA, USA, 2014. http://www.jmol.org/.
(30) Humphrey, W.; Dalke, A.; Schulten, K. VMD: Visual molecular dynamics. *J. Mol. Graphics* **1996**, *14* (1), 33−38.
(31) (a) Häussermann, U.; Wengert, S.; Hofmann, P.; Savin, A.; Jepsen, O.; Nesper, R. Localization of Electrons in Intermetallic Phases Containing Aluminum. *Angew. Chem., Int. Ed. Engl.* **1994**, *33* (20), 2069−2073. (b) Silvi, B.; Savin, A. Classification of chemical bonds based on topological analysis of electron localization functions. *Nature* **1994**, *371* (6499), 683−686.
(32) Silvi, B. The synaptic order: a key concept to understand multicenter bonding. *J. Mol. Struct.* **2002**, *614* (1−3), 3−10.
(33) (a) Abraham, R.; Marsden, J. E. *Foundations of Mechanics*; American Mathematical Society: New York, NY, USA, 1978. (b) Abraham, R.; Shaw, C. D. *Dynamics—the Geometry of Behavior: Global Behavior*. Aerial Press: Santa Cruz, CA, USA, 1985.
(34) Silvi, B.; Pilme, J.; Fuster, F.; Alikhani, M. E. What can Tell Topological Approaches on the Bonding in Transition Metal Compounds. In *Metal-Ligand Interactions*; Russo, N.; Salahub, D.; Witko, M., Eds.; Kluwer Academic Publishers: Dordrecht, Netherlands, 2003; Vol. *116*, pp 241−284.
(35) Dietl, N.; Schlangen, M.; Schwarz, H. Thermal Hydrogen-Atom Transfer from Methane: The Role of Radicals and Spin States in Oxo-Cluster Chemistry. *Angew. Chem., Int. Ed.* **2012**, *51* (23), 5544−5555.
(36) (a) Shaik, S.; Kumar, D.; de Visser, S. P.; Altun, A.; Thiel, W. Theoretical perspective on the structure and mechanism of cytochrome P450 enzymes. *Chem. Rev.* **2005**, *105* (6), 2279−2328. (b) Shaik, S.; Cohen, S.; Wang, Y.; Chen, H.; Kumar, D.; Thiel, W. P450 Enzymes: Their Structure, Reactivity, and Selectivity-Modeled by QM/MM Calculations. *Chem. Rev.* **2010**, *110* (2), 949−1017.
(37) Lai, W.; Chen, H.; Cohen, S.; Shaik, S. Will P450cam Hydroxylate or Desaturate Alkanes? QM and QM/MM Studies. *J. Phys. Chem. Lett.* **2011**, *2* (17), 2229−2235.
(38) Shaik, S.; Hirao, H.; Kumar, D. Reactivity of high-valent iron-oxo species in enzymes and synthetic reagents: A tale of many states. *Acc. Chem. Res.* **2007**, *40* (7), 532−542.
(39) Viciano, I.; Castillo, R.; Martí, S. QM/MM modelling of the hydroxylation of the androstenedione substrate catalyzed by Cytochrome P450 Aromatase (CYP19A1). Submitted for publication in *J. Comput. Chem.*
(40) Stone, K. L.; Behan, R. K.; Green, M. T. X-ray absorption spectroscopy of chloroperoxidase compound I: Insight into the reactive intermediate of P450 chemistry. *Proc. Natl. Acad. Sci. U. S. A.* **2005**, *102* (46), 16563−16565.
(41) (a) Melin, J.; Fuentealba, P. Application of the electron localization function to radical systems. *Int. J. Quantum Chem.* **2003**, *92* (4), 381−390. (b) Polo, V.; Andrés, J. A joint study based on the electron localization function and catastrophe theory of the chameleonic and centauric models for the Cope rearrangement of 1,5-hexadiene and its cyano derivatives. *J. Comput. Chem.* **2005**, *26* (14), 1427−1437. (c) Polo, V.; Andres, J.; Castillo, R.; Berski, S.; Silvi, B. Understanding the Molecular Mechanism of the 1,3-Dipolar Cycloaddition between Fulminic Acid and Acetylene in Terms of the Electron Localization Function and Catastrophe Theory. *Chem.—Eur. J.* **2004**, *10* (20), 5165−5172.

DOI: 10.1021/ct501030q
J. Chem. Theory Comput. 2015, 11, 1470−1480